AGU PUBLICATIONS

Geophysical Research Letters

RESEARCH LETTER
10.1002/2017GL074502

Key Points:
- The Geodetic Alarm System satisfactorily recovers magnitude and fault length for 1300 synthetic Cascadia subduction zone earthquakes
- An end-to-end test of the ShakeAlert system demonstrates the need for GNSS data to accurately estimate ground motions in real time

Supporting Information:
- Supporting Information S1
- Movie S1

Correspondence to:
C. J. Ruhl,
cruhl@berkeley.edu

Citation:
Ruhl, C. J., D. Melgar, R. Grapenthin, and R. M. Allen (2017), The value of real-time GNSS to earthquake early warning, *Geophys. Res. Lett.*, *44*, 8311–8319, doi:10.1002/2017GL074502.

Received 7 JUN 2017
Accepted 10 AUG 2017
Accepted article online 15 AUG 2017
Published online 26 AUG 2017

The value of real-time GNSS to earthquake early warning

C. J. Ruhl[1], D. Melgar[1], R. Grapenthin[2], and R. M. Allen[1]

[1]UC Berkeley Seismological Laboratory, University of California, Berkeley, Berkeley, California, USA, [2]New Mexico Institute of Mining and Technology, Socorro, New Mexico, USA

Abstract Global Navigation Satellite Systems (GNSS)-based earthquake early warning (EEW) algorithms estimate fault finiteness and unsaturated moment magnitude for the largest, most damaging earthquakes. Because large events are infrequent, algorithms are not regularly exercised and insufficiently tested on few available data sets. We use 1300 realistic, time-dependent, synthetic earthquakes on the Cascadia megathrust to rigorously test the Geodetic Alarm System. Solutions are reliable once six GNSS stations report static offsets, which we require for a "first alert." Median magnitude and length errors are −0.15 ± 0.24 units and −31 ± 40% for the first alert, and −0.04 ± 0.11 units and +7 ± 31% for the final solution. We perform a coupled test of a seismic-geodetic EEW system using synthetic waveforms for a M_w8.7 scenario. Seismic point-source solutions result in severely underestimated peak ground acceleration. Geodetic finite-fault solutions provide more accurate predictions at larger distances, thus increasing warning times. Hence, GNSS observations are essential in EEW to accurately characterize large (out-of-network) events and correctly predict ground motion.

Plain Language Summary Earthquake early warning algorithms that use ground motion data measured by the Global Navigation Satellite System (GNSS) complement traditional seismic approaches. GNSS instruments, unlike seismometers, reliably record permanent ground movement. These data enable reliable estimation of total fault length and magnitude for the largest earthquakes. As there are not many large earthquakes, the system is not tested regularly. We use computer-simulated earthquake scenarios to test the Geodetic Alarm System, a GNSS-based algorithm developed for the western U.S. The Geodetic Alarm System satisfactorily recovers magnitude and fault length for 1300 synthetic earthquakes. The fault solutions provide more accurate predictions of ground shaking than seismic algorithms. We demonstrate that GNSS observations are essential in earthquake early warning to accurately characterize large events and correctly predict ground shaking.

1. Introduction

Earthquake early warning (EEW) systems are designed to provide warning before the onset of strong ground shaking as quickly and accurately as possible after an event initiates [*Allen et al.*, 2009a]. Traditionally, such systems use features of elastic waves recorded on seismometers to estimate the magnitude and epicenter location. For example, the ShakeAlert EEW system operating in the U.S. uses a combination of the amplitude and frequency content of the first few seconds of the *P* wave arrival to estimate source information. A ground motion prediction equation (GMPE) then estimates shaking intensity at specific locations. An inherent problem with inertial sensors used by EEW algorithms is low fidelity measurement of very low frequency displacements [*Boore and Bommer*, 2005; *Melgar et al.*, 2013]; furthermore, the first few seconds of the *P* wave, as recorded by inertial sensors, do not contain enough information to forecast growth of the earthquake into a very large *M*8+ event [*Meier et al.*, 2016]. This leads to magnitude saturation, a well-documented condition for large earthquakes whereby an EEW system underestimates the true event magnitude. Most notably, during the 2011 M_w9.0 Tohoku-Oki, Japan earthquake, first and final alerts issued 8.6 and 116.8 s after origin time underestimated the magnitude as M_w7.2 and M_w8.1, respectively [*Hoshiba et al.*, 2011]. As a result, ground motions in the greater Tokyo area were underestimated and tsunami warnings, which rely on these magnitude estimates, while timely, severely underestimated the tsunami intensity [*Hoshiba and Ozaki*, 2014].

Another difficulty faced by seismic systems are large out-of-network events. The performance of seismic point-source (e.g., ElarmS) [*Allen et al.*, 2009b] and seismic finite-fault algorithms (e.g., Finder) [*Böse et al.*, 2012]

during replays of the out-of-network M_w7.2 El Mayor-Cucapah event show poor magnitude and location estimation when using only the stations operating in real time.

Global Navigation Satellite Systems (GNSS) can be conceptualized as a strong motion displacement sensor capable of measuring long periods down to the static offset (0 Hz) [*Melgar et al*., 2013] and thus can ameliorate some of these issues. The notion of utilizing geodetic measurements for rapid source estimation was first proposed by *Blewitt et al*. [2006] following the 2004 M_w9.3 Sumatra earthquake. While no EEW system was in place for that event, global networks relying on long-period seismic observations underestimated the event magnitude at M_w8.0–8.5 within the first hour. *Sobolev et al*. [2007] argued that a GNSS-based system was fundamental for local tsunami warning. *Crowell et al*. [2009] then demonstrated operationally how real-time GNSS could be used for fast magnitude calculations. Many incremental improvements have been made since then, and many techniques have been proposed for using GNSS to quickly estimate source properties, a review of these can be found in *Bock and Melgar* [2016].

On the basis of these findings, and in an attempt to provide coverage for the full range of damaging magnitudes (*M*6+), several groups in the U.S. have developed EEW algorithms that rely on geodetic data over the last decade. Three of these are being tested for implementation into ShakeAlert. *Minson et al*. [2014] proposed the BEFORES (Bayesian Evidence-based Fault Orientation and Real-time Earthquake Slip) inversion strategy to evaluate a suite of potential fault orientations, select the most likely solution, and report the magnitude, spatial distribution of slip, and fault geometry of the model. More recently, *Crowell et al*. [2016] demonstrated a two-part prototype system, the G-FAST system, which provides robust estimates of magnitude and timing from peak ground displacement scaling and solves for the Centroid Moment Tensor and for slip on a finite fault. The third algorithm, and the focus of this paper, is the Geodetic Alarm System (G-larmS). This was the first operational real-time geodetic system in the United States [*Grapenthin et al*., 2014a]. G-larmS analyzes GNSS position time series in real time, determines static offsets, and performs a least squares inversion for slip using a priori fault geometries centered on the epicenter provided by the ShakeAlert seismic algorithms [*Colombelli et al*., 2013]. G-larmS produced accurate simulated real-time and true real-time solutions at 36 s and 14 s after origin time for the out-of-network 2010 M_w7.2 El Mayor-Cucapah (Figure S1) and the 2014 M_w6.0 Napa earthquakes, respectively [*Grapenthin et al*., 2014a, 2014b]. The 2014 Napa earthquake was the first and only earthquake large enough to exercise G-larmS in real time in 3.5 years of operational testing.

Recent advances in and testing of these systems are encouraging and demonstrated the capability of GNSS-based EEW to overcome magnitude saturation, resolve out-of-network events, and determine fault finiteness and slip distributions. Unfortunately, large earthquakes are rare and high-rate, real-time GNSS networks are relatively young and their data not always open; most systems have only been evaluated using a limited number of test cases. It has been difficult to assess the true real-time performance of these approaches. For testing purposes, *Melgar et al*. [2016] developed a methodology to generate synthetic kinematic large earthquakes on finite faults and resulting high-rate GNSS data. In this paper, we will use a suite of 1300 M_w7.8–9.2 Cascadia Subduction zone (CSZ) simulations to determine the performance of G-larmS. We will systematically study the ability of the algorithm for recovering magnitude, fault length, and predicted ground motion. Finally, because G-larmS is coupled to the seismic point-source algorithms of ShakeAlert, we will demonstrate end-to-end testing of the system with one M_w8.7 scenario for which we have calculated broadband waveforms for seismic and geodetic sites. We will show that the additional information and accuracy achieved by using available real-time GNSS data has substantial added value and that geodesy has an important role to play in providing warnings for the largest, most damaging earthquakes and their associated hazards.

2. The Geodetic Alarm System

G-larmS integrates real-time GNSS into earthquake early warning systems [*Grapenthin et al*., 2014a]. In its current implementation, G-larmS continuously analyzes positioning time series and is capable of ingesting both relative displacements (baselines) and absolute positions from precise point positioning solutions. Because GNSS data are comparatively noisy, G-larmS was designed to use triggers from the more sensitive seismic system, though *S* wave based triggering, particularly in sparse seismic networks, is a possible addition to the overall EEW system [*Ohta et al*., 2012; *Grapenthin et al*., 2017]. During an earthquake, the ShakeAlert seismic system issues event messages containing hypocenter and origin time that trigger G-larmS. The algorithm

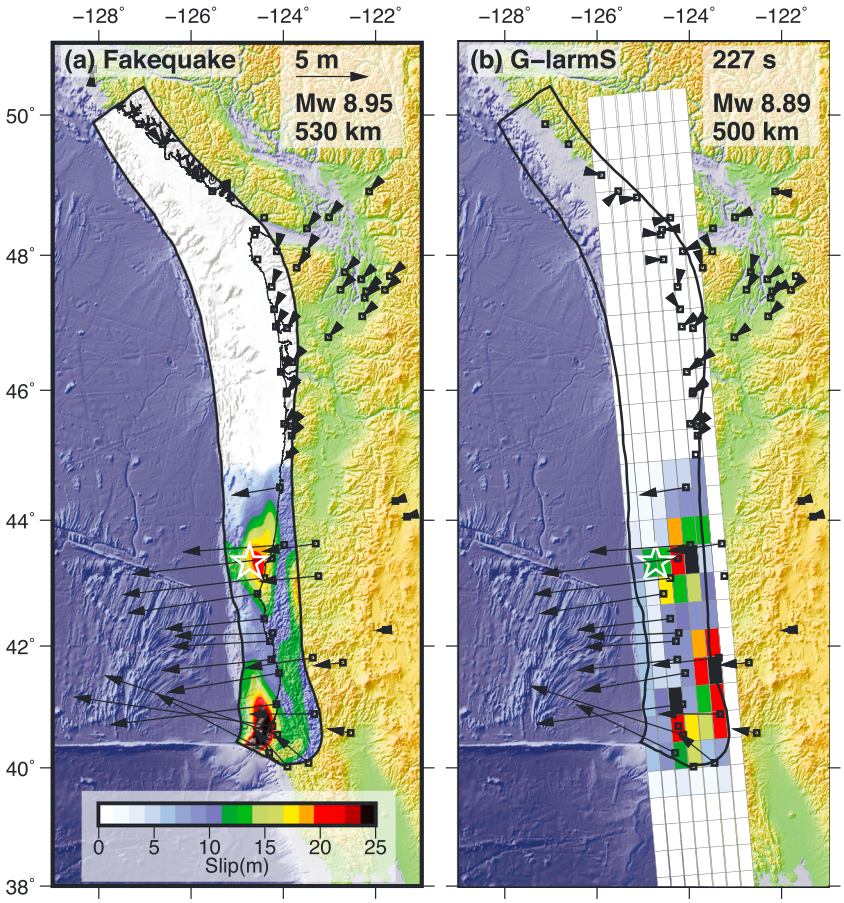

Figure 1. Example slip pattern and static offsets (black arrows) for (a) *M*8.95 fakequake and (b) recovered G-larmS solution. Black outline shows slab boundaries. Fakequake hypocenter shown by white star.

estimates static offsets epoch-by-epoch at each site. Simultaneously, it inverts these static offsets for distributed slip on a finite fault. G-larmS centers the model fault plane on the earthquake hypocenter provided by ShakeAlert and allows the fault to grow based on scaling relationships [*Wells and Coppersmith*, 1994]. Model fault plane orientations are predefined for tectonic regimes. This means that for instance, for the CSZ, slip will be modeled on three potential low-angle thrust geometries with varying strike, to account for the 3-D geometry of the megathrust. At each epoch, the geometry that minimizes the data residuals is the preferred solution. A detailed description of the algorithm can be found in *Grapenthin et al.* [2014a, 2014b].

3. Testing the Performance of G-larmS Using Fakequakes

We test G-larmS using a catalog of synthetic rupture scenarios on the CSZ generated with the Fakequake algorithm for synthetic events and waveform simulation [*Melgar et al.*, 2016]. Stochastic static slip distributions are generated using the Karhunen-Loève expansion [*LeVeque et al.*, 2016], kinematic parameters are then defined following *Graves and Pitarka* [2010], and 1 sps GNSS displacements are synthesized using a Green's function approach. Using this method, *Melgar et al.* [2016] developed 1300 kinematic slip distributions and 1 sps displacement waveforms at the locations of 62 real time, continuous GNSS sites in the Pacific Northwest (Figure 1a). Moment magnitudes for the events range from 7.8 to 9.2, with variable lengths, widths, slip distributions, and hypocentral positions per target magnitude. All fakequakes are pure reverse dip slip and use a 3-D curving slab geometry with variable strike and dip [*Hayes et al.*, 2012]. Events were designed with large variability in order to test the limits of G-larmS and study its response to both expected and unexpected events of varying complexity.

Novel to this paper, we also perform an end-to-end test of the ShakeAlert system using one broadband fakequake (Figures 1a and S2). For this M_w8.7 event, in addition to the 1 sps GNSS data, we generated three-component 100 sps accelerograms at the locations of 40 ShakeAlert stations (Figures 1 and S3). The procedure was as follows: the kinematic source and low-frequency acceleration time series were generated using the Fakequakes code; high-frequency time series were generated using the semistochastic method of *Graves and Pitarka* [2015] as implemented in the SCEC broadband platform software [*Maechling et al*., 2015] and then combined using a 1 Hz corner matched filter.

We trigger G-larmS using a ShakeAlert-style message containing the exact fakequake hypocenter and an initial magnitude estimate of 6.0. Noise is added to the simulated displacement waveforms, and then offsets are estimated on the noisy data at each epoch for a total of 5 min. In Cascadia, G-larmS solves for slip on three possible planar megathrust geometries with strike and dip as follows: north (320°,12°), nouth (355°,12°), and average (338°,12°). Subfault patch sizes are fixed at 50 km length by 25 km width, except in the case of the broadband fakequake in which we use a width of 50 km to speed up Green's function calculation when adding new patches. Fault growth is confined to within the seismogenic zone between 5 and 30 km depth. We use a fixed regularization factor for all 1300 rupture scenarios regardless of magnitude. Parameter estimation runs in simulated real time for 3 min following origin time producing finite fault slip solutions every epoch after the first *S* wave arrival at the nearest site (V_S = 3.2 km/s). An example of the static offsets and slip distribution recovered by G-larmS for one of the scenarios at 230 s after OT is shown side by side with the fakequake rupture in Figure 1b.

For the end-to-end broadband simulation, we first replay the accelerograms through ElarmS. This results in estimates of hypocentral location and magnitude (Figure S2), which are then used by GlarmS to determine finite-fault slip; to run in parallel in real time is easily done.

4. Evaluation Metrics

We evaluate the ability of G-larmS to compute magnitude and fault length. Magnitude is calculated by G-larmS based on fault area, slip, and an assumed rigidity of 30 GPa. We compare G-larmS magnitudes to the known fakequake magnitudes (Figure 2). For a heterogeneous three-dimensional slip distribution, fault length can be subjective. In this work, we modify the concept of effective length from *Mai and Beroza* [2000]. Lengths are estimated in two ways: for the fakequakes they are calculated using the smallest extent along strike that includes both the hypocenter and all subfault patches with slip ≥80% of the mean of nonzero slip or 5 m, whichever is smaller. G-larmS lengths are best represented using a threshold of 10% of the max slip or 5 m, whichever is smaller. This difference is likely due to the different subfault discretizations; fakequakes have smaller subfaults and thus a larger variability of slip distributions with higher peak slip than the bigger subfaults of, and therefore smoother, G-larmS solutions.

5. Results

We describe qualification and timing of the G-larmS first alert and then assess the results for the above metrics for first and final alerts. We discuss the results for the GNSS-only fakequakes and then use the end-to-end test with the broadband fakequake to demonstrate the value added by the geodetic algorithm.

5.1. Determining the Geodetic First Alert

To reconcile spurious triggers, seismic point-source algorithms (e.g., ElarmS) require a minimum number of stations (2–4) to trigger before issuing an alert. While G-larmS is triggered after the ShakeAlert system has already determined that an earthquake is occurring, it is of great value to understand how many stations with static offset estimates are required to obtain good finite-fault solutions. For the Cascadia test suite, we use the magnitude residual (true minus predicted magnitude) to make this assessment. We show that a minimum of six stations is necessary to achieve a mean magnitude error less than or equal to 0.3 using the current station geometry (Figure S5). Hence, six stations measuring a static offset are our criterion to determine the geodetic "first alert" time, length, and magnitude from G-larmS. The median time to geodetic first alert for all simulations is 41 ± 14 s(1σ) from origin time (Figure 2a). We note that G-larmS is configured to wait until a theoretical *S* wavefront arrives at a site before estimating offsets and including that site in the inversion. For near-trench offshore Cascadia events, *S* waves arrive at ~20s for coastal sites closest to the hypocenter, and the six-station

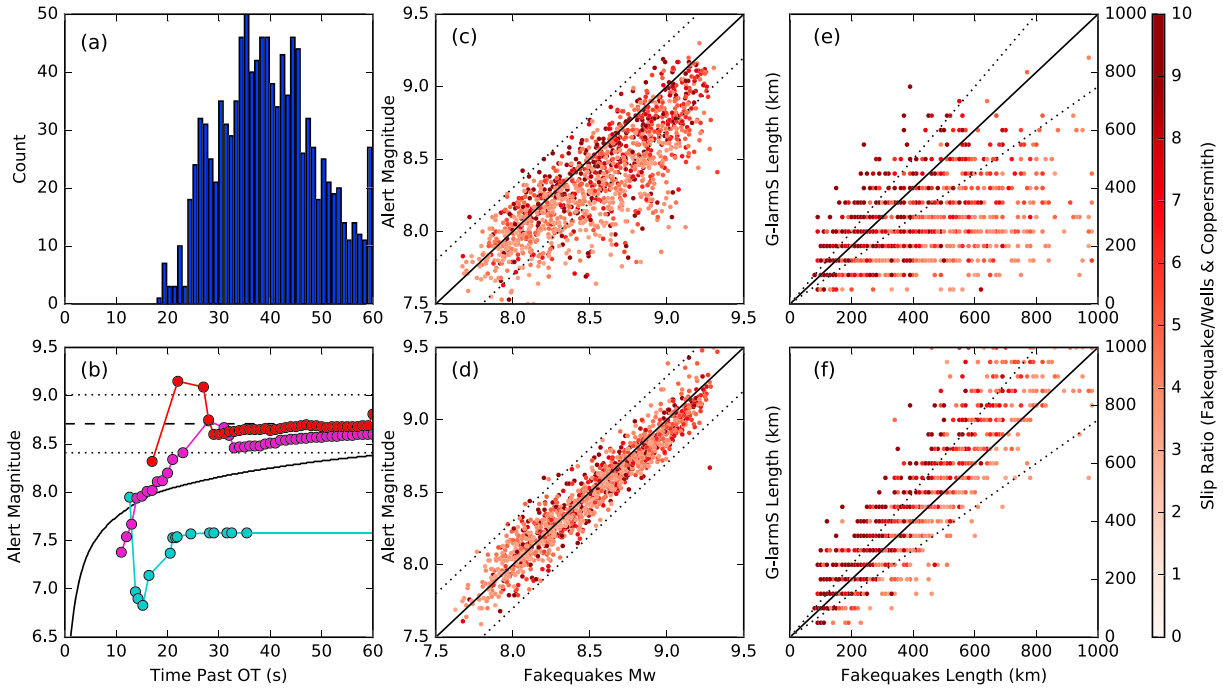

Figure 2. Synthesis of G-larmS results. (a) Histogram of 1300 geodetic first alert times. (b) Alert magnitude evolution relative to origin time (OT) for the single broadband fakequake scenario run (ElarmS-cyan and G-larmS *S/P* wave—red/magenta). The magnitude (dashed line) and cumulative moment magnitude (solid) of the fakequake are shown. Dotted lines show ±0.3 units (Figures 2d–2d) and ±25% length (Figures 2e and 2f). (c, d) Magnitude and (e, f) fault length comparison plots for geodetic first alerts (Figures 2c and 2e) and final solutions (Figures 2d and 2f). Colors indicate ratio of maximum slip in each fakequake over the expected maximum slip based on the fakequake fault length and *Wells and Coppersmith* [1994]. Solid lines show a ratio of 1:1.

requirement adds to the time for the geodetic first alert. Onshore events and deeper Cascadia events closer to the coast will have faster G-larmS alert times.

5.2. Length and Magnitude

First and final magnitude and fault length estimates for all 1300 scenarios are shown in Figures 2c and 2d, respectively. The magnitude solutions center around a 1:1 line and median errors for the geodetic first and final alerts are −0.15 ± 0.24 and −0.04 ± 0.11 magnitude units, respectively (Figures 2c and 2d). There is an overall pattern that initial fault solutions are on average 31% shorter than the fakequakes length, with large scatter (Figure 2e). By contrast the final solutions are closer to the true length on average overestimating them by 7.1 ± 31% (Figure 2f). Length estimates are affected by earthquake complexities present in fakequake simulations and in natural earthquakes observed worldwide, such as unilateral rupture and stress drops. As a proxy for stress drop, we use the ratio of maximum fault slip in each fakequake and that predicted by *Wells and Coppersmith* [1994] based on the fakequake fault length. Fault lengths for events with large slip ratios (i.e., high concentration of slip over a smaller area) are systematically overestimated for both first and final alerts (Figures 2e and 2f). In contrast, the length of unilateral ruptures is sometimes underestimated due to total fault length limits coupled with the symmetrical fault growth approach taken by G-larmS.

5.3. M_w8.7 Broadband Simulation Results

The M_w8.7 broadband fakequake illustrates the time progression of alerts likely to occur in the fully coupled seismic/geodetic system (Figure 2b). A timeline of alerts and corresponding ground motion prediction maps are shown in Figure 3. The ElarmS first alert at 12.4 s has a magnitude error of −0.8 units and is located ~20 km seaward of the fakequake hypocenter. To improve the G-larmS alert time, we initiated offset estimation upon predicted *P* wave arrival assuming a velocity of 5.5 km/s, rather than predicted *S* wave arrival, thus producing the first G-larmS alert at 16 s, rather than 28 s (Figures 3 and S4). Earlier offset estimation dampens the impact of dynamic oscillations arriving with the *S* wave, initially underestimating the growing offset and slightly increasing the time of convergence to final displacements (e.g., Figures S4 and 1 in *Melgar et al.* [2012]).

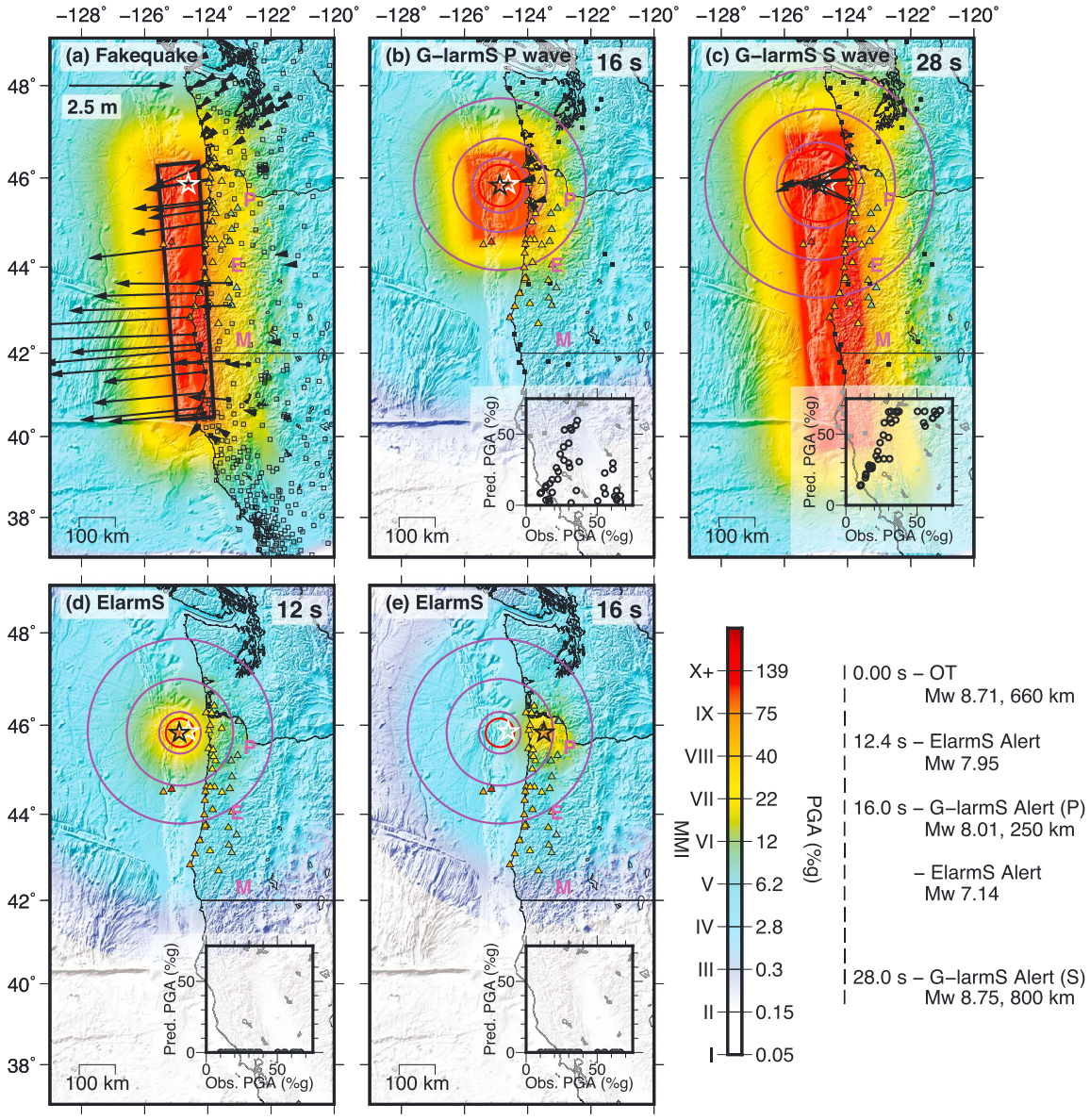

Figure 3. Shaking intensity maps produced from (a) the *M*8.7 broadband fakequake, the G-larmS alerts at (b) 16 s and (c) 28 s, and the ElarmS alerts at (d) 12 s and (e) 16 s. The fakequake hypocenter (white star), alert hypocenter (black star), seismic stations colored by fakequake PGA (triangles), and used (solid squares) and existing (hollow square) GNSS stations are shown. The *S* wave distance at 0 (gray), 5, 30, and 60 s (purple) after the alert time is shown by concentric circles. G-larmS static offsets (black arrows) are shown (Figures 3b and 3c). PGA measured from fakequakes' waveforms and predicted PGA are compared in the insets for each panel; Portland (P), Eugene (E), and Medford (M), Oregon are labeled for discussion. Timeline shown at right.

Offset estimation that starts with the *S* wave arrival depends significantly on the assumed velocity, which may introduce delays if underestimated. Balancing this trade-off requires future work.

The finite-fault model based on the predicted *S* wave arrival (Figures 1 and 3c) at 28 s has a magnitude error of <0.1 units and a length error of +150 km (+23%), showing improvement over the shorter, lower magnitude solution at 16 s that started with the predicted *P* wave arrival (Figure 3b). The inversion is better constrained as more data become available. Figure 3c shows that we accurately infer the final extent of the fault using only the first ~100 km of rupture (demarcated by offsets in Figure 3c) as early as 28 s after rupture initiation. *Melgar et al.* [2015] demonstrated that accurate magnitudes can be estimated from displacement data before rupture completion for great earthquake worldwide. For example, magnitudes converge as early as 40 s for the 200 s—long rupture of the *M*8.8 Maule, Chile earthquake. This is ultimately driven by moment release and

rupture propagation. As discussed below, the improved fault model at 28 s leads to substantial differences in the estimated ground motions.

6. Discussion

Our results show that G-larmS is performing well when estimating the earthquake magnitude and length for a complex array of slip distributions under simplifying assumptions. However, the goal of EEW is to provide warning in advance of ground shaking. Thus, to further demonstrate the importance of GNSS utilization in EEW, we use the broadband fakequake event to showcase the improvements to ground motion estimation GNSS brings. GMPEs translate source information to expected shaking intensities and rely fundamentally on the earthquake magnitude, and its distance from a particular location at which ground motion is estimated. For small events, fault finiteness can be neglected and the hypocentral or epicentral distance is used. However, depending on observation distance, when ruptures grow to tens or hundreds of kilometers, this assumption is no longer useful for predicting shaking intensity because a given location can be far from the hypocenter yet close to the rupture.

Consider Figure 3, where we show maps of predicted peak ground acceleration (PGA) for the broadband fakequake constructed using the *Boore et al*. [2014] GMPE. Moderate to strong shaking of Modified Mercalli Intensity (MMI) V-VI in the Portland area (Figure 3a) is underestimated by the point-source solutions (Figures 3d and 3e) as MMI II-IV (weak to very light shaking). The finite-fault solutions accurately reproduce the expected shaking at both 16 s and 28 s (Figures 3b and 3c). The first seismic-only alert at 12 s provides warning times of 37, 62, and 119 s to the Portland, Eugene, and Medford, OR population centers, respectively. Portland, OR is the closest and largest of these cities located at 156 km distance with a greater metropolitan area population of over 2.3 M people. A 28 s alert would still provide warning of 21 s to the Portland area, and more accurate ground motions would be especially important for coastal areas along the extent of rupture. For instance, ElarmS' first and 16 s alerts would not warn parts of Northern California that would actually experience severe shaking greater than MMI VIII. Testing of the coupled seismic-geodetic system with broadband scenarios is thus important and illuminating. In forthcoming work, we will systematically explore the performance with a larger suite of such scenarios.

First alerts generally occur before the source process is complete. For the broadband fakequake, for example, the first alert time is 28 s, slightly lower than the median of 41+/−14 s for the remaining 1300 scenarios. In spite of the source not having ruptured completely, the magnitude estimates are fairly stable (Figure 2b). Figures 2c and 2e show that while sometimes first alerts are close to the final magnitude, they are generally biased low, likely because static offsets are not fully developed or discernible. However, when large dynamic motions and static offsets develop early on in the source process, the still underconstrained inversion smears large localized slip over a much broader area. In particular, large dynamic motions at stations close to the hypocenter, as in our broadband fakequake example, will emphasize this effect. This has the positive side effect of leading to estimates of rupture length longer than what has currently ruptured. In turn, this calculation of length leads to better estimates of expected ground motions early on. Of course, an earthquake with large slip over a small area would, in turn, result in an overprediction of shaking at far distances.

An important question is whether the current operational real-time GNSS network provides adequate coverage. In section 5.1, we discussed our design goal of achieving mean magnitude errors of ±0.3 and concluded that G-larmS requires at least six stations to measure coseismic offsets to achieve this (Figure S5). To test current network capabilities, we perform a simple calculation: we simulate offsets everywhere in the Pacific Northwest for a uniform-slip finite-extent M_w7.0 thrust earthquake oriented at 355°,15° and centered at 15 km depth. We shifted the origin of this test event on a regular grid and calculated the number of stations that would record at least 2.0 cm static offset, consistent with the expected noise of real-time solutions [e.g., *Genrich and Bock*, 2006]. The results for three network configurations are shown in Figure 4. Events occurring inside the six-station contour would be observed by at least six sites and thus expected to be within the ±0.3 magnitude error. Note that there is no time dependence; we analyze this for total static offsets. Figure 4a shows the results using 62 roughly evenly spaced GNSS stations concentrated along the coastline of the Pacific Northwest. This configuration reflects the real-time stations used by the G-larmS demonstration system today and only provides sufficient coverage for the Seattle-Tacoma area of Washington. Figure 4b shows the results if all currently operating real-time GNSS stations from the Pacific Northwest Geodetic Array

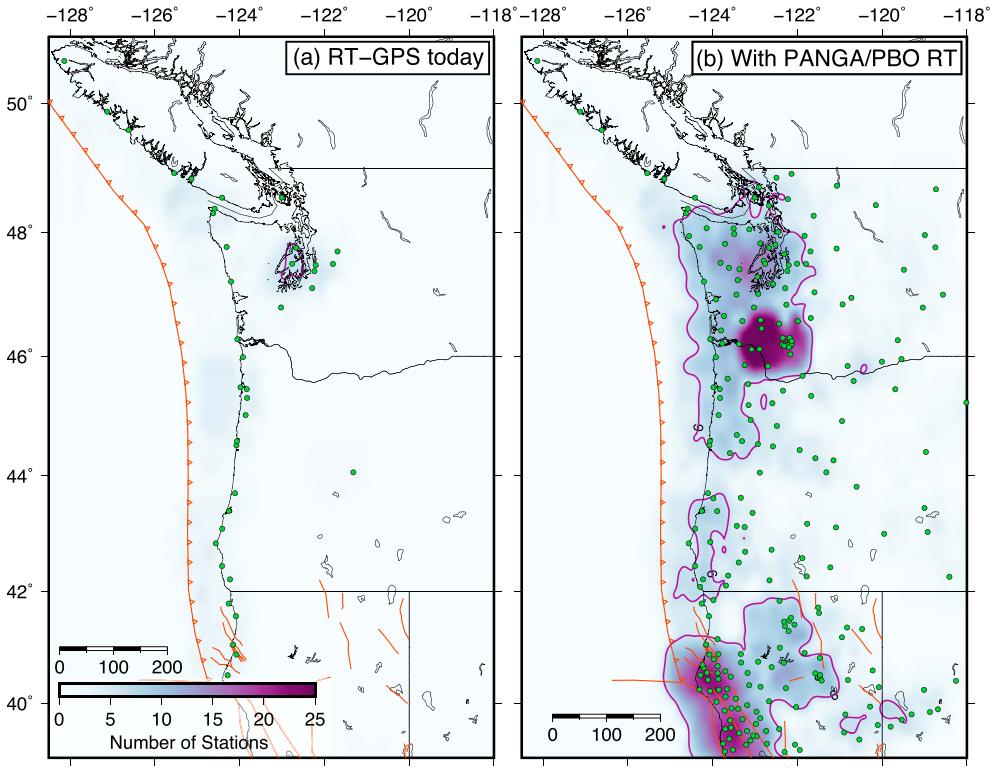

Figure 4. GNSS network sensitivity maps for the Pacific Northwest. Histogram maps of number of stations (green circles) detecting displacements greater than or equal to 2.0 cm from a *M*7.0 earthquake using (a) only current real-time (RT) GNSS stations imported and used by G-larmS, and (b) using all GNSS stations that currently have RT capabilities. Quaternary faults are shown by red lines. The six-station contours are the purple lines.

(PANGA) and the Plate Boundary Observatory (PBO) were integrated into the system. Adequate EEW coverage would be expanded to all major metropolitan areas in the Northwestern U.S. This suggests that no major network upgrades are necessary; simply ingesting existing data streams would suffice. The only area where denser station coverage would be beneficial is Vancouver Island. We also estimated the optimal interstation spacing for detecting and accurately modeling M_w7+ events in the CSZ. We created synthetic distributions of GNSS stations, regularly spaced at different intervals and calculated how many stations exceeded the same 2.0 cm static offset threshold (Figure S6). The results suggest an optimal station spacing of 35 km. In addition, G-larmS results for synthetic earthquakes with magnitudes greater than 7.5 (Figures 2 and S7) are well resolved with only a subset of the current system stations. Overall, this suggests that improvements are possible but that coverage is sufficient for the largest megathrust events.

7. Conclusions

Including GNSS-based finite-fault inversion algorithms in EEW is essential to overcoming magnitude saturation, providing coverage for out-of-network events, and estimating fault finiteness required to accurately determine ground motions for the largest events. Here we rigorously tested the Geodetic Alarm System using synthetic earthquakes on the Cascadia subduction zone and demonstrated that GNSS can contribute to a comprehensive EEW system. The system performed well for the 1300, sometimes extreme, scenarios with median magnitude and length errors of −0.15 units and −30% for the first alerts, and −0.04 units and +7% for the final alerts, respectively. We further performed an end-to-end test of the ShakeAlert system using an M_w8.7 broadband Cascadia earthquake scenario. Ground motions predicted from the point-source solutions at 12 and 16 s severely underestimate PGA, while the finite-fault solutions at 16 s and, particularly, at 28 s provide substantially improved, more accurate warnings at larger distances and with sufficient warning time. Together, this comprehensive set of tests and simulation results strongly argue that GNSS should play a fundamental role in a modern earthquake early warning system.

Acknowledgments
This work was funded by the Gordon and Betty Moore Foundation through grant GBMF3024 to UC Berkeley and the U.S. Geological Survey grants G15 AC00331 and G16 AC00348. The data used in this study were produced by *Melgar et al*. [2016] and can be accessed at https://zenodo.org/record/59943 or reproduced with the Fakequakes code at https://www.github.com/dmelgarm/MudPy.

References

Allen, R. M., H. Brown, M. Hellweg, O. Khainovski, P. Lombard, and D. Neuhauser (2009a), Real-time earthquake detection and hazard assessment by ElarmS across California, *Geophys. Res. Lett.*, *36*, L00B08, doi:10.1029/2008GL036766.

Allen, R. M., P. Gasparini, O. Kamigaichi, and M. Bose (2009b), The status of earthquake early warning around the world: An introductory overview, *Seismol. Res. Lett.*, *80*(5), 682–693.

Blewitt, G., C. Kreemer, W. C. Hammond, H. Plag, S. Stein, and E. Okal (2006), Rapid determination of earthquake magnitude using GNSS for tsunami warning systems, *Geophys. Res. Lett.*, *33*, L11309, doi:10.1029/2006GL026145.

Bock, Y., and D. Melgar (2016), Physical applications of GNSS geodesy: A review, *Rep. Prog. Phys.*, *79*(10), doi:10.1088/0034-4885/79/10/106801.

Boore, D. M., and J. J. Bommer (2005), Processing of strong-motion accelerograms: Needs, options and consequences, *Soil Dyn. Earthq. Eng.*, *25*(2), 93–115.

Boore, D. M., J. P. Stewart, E. Seyhan, and G. M. Atkinson (2014), NGA-West2 equations for predicting PGA, PGV, and 5% damped PSA for shallow crustal earthquakes, *Earthquake Spectra*, *30*(3), 1057–1085.

Böse, M., T. Heaton, and E. Hauksson (2012), Rapid estimation of earthquake source and ground-motion parameters for earthquake early warning using data from a single three-component broadband or strong-motion sensor, *Bull. Seismol. Soc. Am.*, *102*(2), 738–750.

Colombelli, S., R. M. Allen, and A. Zollo (2013), Application of real-time GNSS to earthquake early warning in subduction and strike-slip environments, *J. Geophys. Res. Solid Earth*, *118*, 3448–3461, doi:10.1002/jgrb.50242.

Crowell, B. W., Y. Bock, and M. B. Squibb (2009), Demonstration of earthquake early warning using total displacement waveforms from real-time GNSS networks, *Seismol. Res. Lett.*, *80*(5), 772–782.

Crowell, B. W., et al. (2016), Demonstration of the Cascadia G-FAST geodetic earthquake early warning system for the Nisqually, Washington, earthquake, *Seismol. Res. Lett.*, *87*(4), doi:10.1785/0220150255.

Genrich, J. F., and Y. Bock (2006), Instantaneous geodetic positioning with 10–50 Hz GNSS measurements: Noise characteristics and implications for monitoring networks, *J. Geophys. Res.*, *111*, B03403, doi:10.1029/2005JB003617.

Grapenthin, R., I. A. Johanson, and R. M. Allen (2014a), Operational real-time GNSS-enhanced earthquake early warning, *J. Geophys. Res. Solid Earth*, *119*, 7944–7965, doi:10.1002/2014JB011400.

Grapenthin, R., I. A. Johanson, and R. M. Allen (2014b), The 2014 M_w 6.0 Napa earthquake, California: Observations from real-time GNSS-enhanced earthquake early warning, *Geophys. Res. Lett.*, *41*, 8269–8276, doi:10.1002/2014GL061923.

Grapenthin, R., M. West, and J. Freymueller (2017), The utility of GNSS for earthquake early warning in regions with sparse seismic networks, *BSSA*, doi:10.1785/0120160317, in press.

Graves, R. W., and A. Pitarka (2010), Broadband ground-motion simulation using a hybrid approach, *Bull. Seismol. Soc. Am.*, *100*, 2095–2123.

Graves, R., and A. Pitarka (2015), Refinements to the graves and Pitarka (2010), broadband ground-motion simulation method, *Seismol. Res. Lett.*, *86*(1), 75–80.

Hayes, G. P., D. J. Wald, and R. L. Johnson (2012), Slab1.0: A three-dimensional model of global subduction zone geometries, *J. Geophys. Res.*, *117*, B01302, doi:10.1029/2011JB008524.

Hoshiba, M., and T. Ozaki (2014), Earthquake early warning and tsunami warning of the Japan meteorological agency, and their performance in the 2011 off the Pacific coast of Tohoku earthquake (M_w 9.0), in *Early Warning for Geological Disasters*, pp. 1–28, Springer, Berlin.

Hoshiba, M., K. Iwakiri, N. Hayashimoto, T. Shimoyama, K. Hirano, Y. Yamada, Y. Ishigaki, and H. Kikuta (2011), Outline of the 2011 off the Pacific coast of Tohoku earthquake (M_w9.0)—Earthquake early warning and observed seismic intensity, *Earth Planets Space*, *63*, 547–551.

LeVeque, R. J., K. Waagan, F. I. Gonzalez, D. Rim, and G. Lin (2016), Generating random earthquake events for probabilistic tsunami hazard assessment, *Pure Appl. Geophys.*, doi:10.1007/s00024-016-1357-1.

Maechling, P. J., F. Silva, S. Callaghan, and T. H. Jordan (2015), SCEC broadband platform: System architecture and software implementation, *Seismol. Res. Lett.*, *86*(1), doi:10.1785/0220140125.

Mai, P. M., and G. C. Beroza (2000), Source scaling properties from finite-fault-rupture models, *Bull. Seismol. Soc. Am.*, *90*(3), 604–615.

Meier, M. A., T. Heaton, and J. Clinton (2016), Evidence for universal earthquake rupture initiation behavior, *Geophys. Res. Lett.*, *43*, 7991–7996, doi:10.1002/2016GL070081.

Melgar, D., Y. Bock, and B. W. Crowell (2012), Real-time centroid moment tensor determination for large earthquakes from local and regional displacement records, *Geophys. J. Int.*, *188*(2), 703–718.

Melgar, D., Y. Bock, D. Sanchez, and B. W. Crowell (2013), On robust and reliable automated baseline corrections for strong motion seismology, *J. Geophys. Res. Solid Earth*, *118*, 1177–1187, doi:10.1002/jgrb.50135.

Melgar, D., B. W. Crowell, J. Geng, R. M. Allen, Y. Bock, S. Riquelme, E. M. Hill, M. Protti, and A. Ganas (2015), Earthquake magnitude calculation without saturation from the scaling of peak ground displacement, *Geophys. Res. Lett.*, *42*, doi:10.1002/2015GL064278.

Melgar, D., R. J. LeVeque, D. S. Dreger, and R. M. Allen (2016), Kinematic rupture scenarios and synthetic displacement data: An example application to the Cascadia subduction zone, *J. Geophys. Res. Solid Earth.*, *121*, 6658–6674, doi:10.1002/2016JB013314.

Minson, S. E., J. R. Murray, J. O. Langbein, and J. S. Gomberg (2014), Real-time inversions for finite fault slip models and rupture geometry based on high-rate GPS data, *J. Geophys. Res. Solid Earth*, *119*, 3201–3231, doi:10.1002/2013JB010622.

Ohta, Y., et al. (2012), Quasi real-time fault model estimation for near-field tsunami forecasting based on RTK-GNSS analysis: Application to the 2011 Tohoku-Oki earthquake (M_w 9.0), *J. Geophys. Res.*, *117*, B02311, doi:10.1029/2011JB008750.

Sobolev, S. V., A. Y. Babeyko, R. Wang, A. Hoechner, R. Galas, M. Rothacher, D. V. Sein, J. Schroter, J. Lauterjung, and C. Subarya (2007), Tsunami early warning using GNSS-shield arrays, *J. Geophys. Res.*, *112*, B08415, doi:10.1029/2006JB004640.

Wells, D. L., and K. J. Coppersmith (1994), New empirical relationships among magnitude, rupture length, rupture width, rupture area, and surface displacement, *Bull. Seismol. Soc. Am.*, *84*, 974–1002.